

---

## NATURAL ELECTROMAGNETIC OSCILLATIONS IN 4–12 Hz FREQUENCY RANGE AS MEASURED BY SWARM SATELLITES AND CARISMA MAGNETOMETER NETWORK

---

**N.V. Yagova**   
Schmidt Institute of Physics of the Earth RAS,  
Moscow, Russia,  
nyagova@ifz.ru

**E.N. Fedorov**   
Schmidt Institute of Physics of the Earth RAS,  
Moscow, Russia, enfedorov1@yandex.ru

**V.A. Pilipenko**   
Schmidt Institute of Physics of the Earth RAS,  
Moscow, Russia, pilipenko\_va@mail.ru  
Geophysical Center RAS, Moscow, Russia

**N.G. Mazur**   
Schmidt Institute of Physics of the Earth RAS,  
Moscow, Russia, ngmazur@mail.ru

---

**Abstract.** We examine magnetic field variations at 4–12 Hz frequencies in the upper ionosphere and on Earth. The ground response to the coherent oscillations at two SWARM satellites near and above the high frequency boundary of the nominal Pc1 range is studied. We use CARISMA data to analyze ground pulsations. Ionospheric oscillations are predominantly registered at geomagnetic latitudes above 65°, i. e. from the auroral zone to the polar cusp-cleft region. The oscillations at the same frequencies are recorded at auroral and subauroral ground stations at distances from 1500 to 3000 km from satellite footprint. Ratio  $R_{GI}$  of the oscillation amplitude on Earth to that in the ionosphere retrieved from the observed data is compared to the values calculated for a finite radius Alfvén beam incident onto a quasi-

real ionosphere [Fedorov et al., 2018]. Radial distribution of  $R_{GI}$  depends on the oscillation frequency and the altitude distribution of ionospheric parameters controlled mostly by season and local time. The most probable values of  $R_{GI}$  range from  $10^{-3}$  to  $10^{-1}$ . The  $R_{GI}$  values obtained from the observed data agree with model ones at incident beam radius of about several hundred kilometers.

**Keywords:** ionosphere, geomagnetic pulsations, MHD waves.

---

### INTRODUCTION

Pc1 geomagnetic pulsations are a physical manifestation of electromagnetic ion-cyclotron (EMIC) waves. The nominal Pc1 range is between 0.2 and 5 Hz and is limited from above by ion-cyclotron resonance frequencies at the top of the field line. Oscillations of higher frequencies may be linked to sharp magnetospheric compression [Ermakova et al., 2015] or off-equatorial generation [Rème et al., 2001; Allen et al., 2015; Vines et al., 2019]. This frequency range corresponds to higher harmonics of the Ionospheric Alfvén Resonator (IAR) and ionospheric waveguide [Polyakov, Rapoport, 1981; Belyaev et al., 1999], which can distort the spectral composition of Pc1 pulsations when passing through the ionosphere to the Earth surface.

Single-point measurements of magnetic field variations by a low-orbit satellite do not allow us to differentiate oscillations from the spatial structures the satellite passes by. It is impossible to determine the frequency of oscillations in a coordinate system fixed with respect to Earth from such measurements because of the Doppler effect [Le et al., 2011]. Multi-satellite measurements, such as the ST5 and SWARM missions, make it possible to distinguish between spatial structures and oscillations [Engebretson et al., 2008; Olsen et al., 2013].

Data from two closely located SWARM-A/C satellites facilitates the identification of wave UHF disturbances of previously unexplored type — short wave packets in the

range 2.5–10 Hz, i.e. above the nominal Pc1 range [Yagova et al., 2023]. Occurrence maxima and amplitudes of these oscillations correspond to dayside polar cusp-cleft regions. The oscillation frequencies observed match the proton-cyclotron resonance frequency at a distance more than 20° from the equator, which suggests that the source of the oscillations lies in the off-equatorial region of the outer magnetosphere. A smaller maximum at the low-frequency flank of the range considered is observed at geomagnetic latitudes of ~60°, i.e. in the vicinity of the plasmapause. Frequencies of the pulsations in this region are in the high-frequency Pc1 range. Such pulsations regularly occur in this region of geomagnetic latitudes [Yahnin et al., 2007]. For individual events, the pulsations occurred at latitudes above the auroral oval polar boundary. Almost all spectral power of the recorded pulsations is concentrated in transverse components, which is typical of the Alfvén wave structure.

To verify the correctness of the interpretation proposed in [Yagova et al., 2023], ionospheric and ground oscillations should be directly compared, which is the purpose of this work. Since the frequency range above the nominal Pc1 range is of the greatest interest, the range in question is slightly higher than in the previous study — from 4 to 12 Hz. We analyze magnetic field variations in the ionosphere and on Earth, selected from measurements made by two SWARM satellites (A and C). For the magnetic field variations simultaneously detect-

ed in the ionosphere and on Earth, which are coherent at the spectral maximum frequency, the Earth/ionosphere amplitude ratio is compared with the values calculated in the model [Fedorov et al., 2018].

## 1. DATA AND PROCESSING

For the analysis, we have used the same 12 days in September and December 2016 with weak or moderate geomagnetic activity as in [Yagova et al., 2023]. As in the previous study, we have selected intervals for which the spectral power density for at least one component on SWARM-A and the coherence between SWARM-A and -C for one of the component pairs exceeded a given threshold. SWARM A/C are closely located — the distance between them varies from 30 to 200 km, and the orbit height is  $\sim 450$  km. Magnetic field measurement data is available with a time resolution of 0.02 s. To suppress the trends caused primarily by the latitude dependence of the main magnetic field, we made high-pass filtration with a cutoff frequency of 1 Hz.

The magnetic field components were recalculated from the original coordinate system of the satellite NEC (North—East—Center) to the system of geomagnetic coordinates. The adapted GEOPACK code was used to calculate angles between geographic and corrected geomagnetic coordinates [Papitashvili et al., 1997]. To distinguish the component designations from the original ones, we employ the designations  $B_N$  and  $B_E$  with positive direction to the north and east respectively for the meridional and latitudinal components.

To analyze ground pulsations, we have used data from four CARISMA stations, equipped with induction magnetometers with a 100 Hz digitization frequency [Mann et al., 2008]. Coordinates of the stations are listed in Table 1, and Figure 1 gives a schematic map of the stations and satellite footprints for a minute interval of  $\sim 19.5$  UT on December 1, 2016 (day 336) when coherent oscillations were observed by the satellites near  $\Phi=80^\circ$  and by four ground stations (event d4 in Figure 9).

Spectral analysis has been performed using the same technique as in [Yagova et al., 2023]: the Blackman-Tukey method was employed to calculate cross-spectra for  $\tau_s=2.56$  s [Jenkins, Watts, 1972]. At the first stage, we selected events with an over-threshold value of the power spectral density  $PSD$  and spectral coherence  $\gamma^2$  at the spectral maximum frequency for at least one pair of horizontal components in the two satellites. Threshold values were chosen at  $PSD_b=3 \cdot 10^{-5} \text{ nT}^2/\text{Hz}$  and  $\gamma_b^2=0.36$ ; only those intervals were considered for which the difference between geomagnetic latitudes of the satellites  $|\Delta\Phi|>0.2^\circ$ . Magnetic field variations for the

intervals thus selected can be interpreted as oscillations whose frequencies, when recorded by a stationary sensor, will have the same order of magnitude as the frequencies on a satellite.

At the second stage, magnetic field variations were examined on the ground for these intervals. We took the periods during which coherent oscillations were observed, and the distance from a ground station to a satellite footprint did not exceed 3000 km. For the selected oscillations, we analyzed the Earth/ionosphere ratio  $PSD R_{GI}^2$ , which was then used to determine the amplitude ratio  $R_{GI}$  and to compare it with the results of the model calculation. For the cases when a coherent signal was received by two or more stations, we studied the dependence  $R_{GI}(\rho)$ .

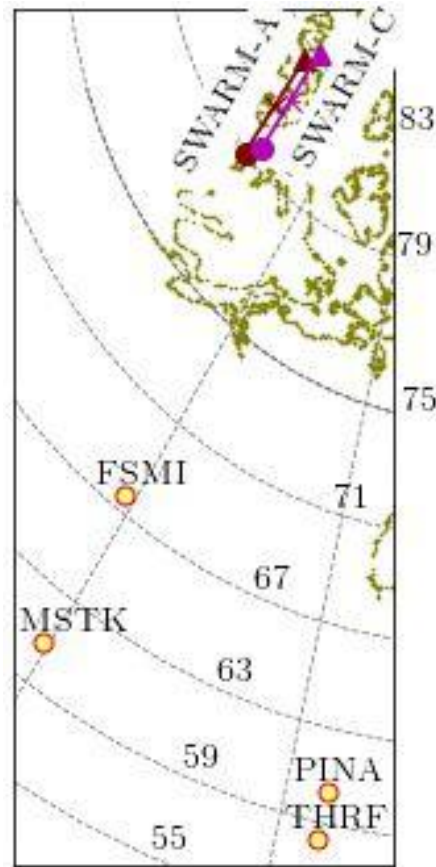


Figure 1. Schematic map of ground stations and satellite footprints for a minute interval in the pre-noon sector ( $MLT \approx 9.5$ ) on December 1, 2016. Crosses mark 19:35:40 UT. The gray dotted line indicates geomagnetic parallels and meridians

Table 1

CARISMA stations

Station code station	Geographic coordinates		Corrected geomagnetic coordinates		Universal time of the local magnetic midnight	Radial distance to the top of the field line, $L$
	latitude	longitude	latitude $\Phi$	longitude $\Lambda$		
	degree		degree			
FSMI	60.017	248.05	67.02	308.82	8.02	6.66
MSTK	53.351	247.03	60.39	309.57	7.99	4.16
PINA	50.199	263.96	59.55	333.17	6.59	3.95
THRF	48.027	263.64	57.41	332.88	6.61	3.50

## 2. RESULTS

### 2.1. Spatial distribution of coherent oscillations

Ground stations occupy magnetic latitudes from  $57^\circ$  to  $67^\circ$ , and the imposed restriction on the distance between the station and the satellite's ground path corresponds to latitudes from  $30^\circ$  to the pole. Figure 2 illustrates the spatial distribution of the occurrence of coherent pulsations  $C_{GI}$ . The value was determined for a cell of corrected geomagnetic (CGM) coordinates  $\Phi$ - $\Lambda$  as the ratio of the total duration of intervals with over-threshold Earth-satellite coherence from at least one pair of horizontal components to the total duration of the intervals for which the spectral analysis was performed. Referring to Figure 2, the coherent oscillations are localized mainly in the geomagnetic latitude region  $\Phi > 60^\circ$ . The occurrence of Hz-range coherent oscillations on the two satellites mainly at high geomagnetic latitudes has been observed in [Yagova et al., 2023]. The distributions shown in Figure 2 are basically similar for FSMI and MSTK stations (auroral and subauroral). For both stations, maximum values of  $C_{GI}$  are approximately 0.25, the main maximum is observed at  $\Phi > 72^\circ$ , and the oscillations almost completely disappear at latitudes below  $50^\circ$ . Both stations recorded a maximum near them and a system of maxima and minima with a spatial quasi-period of  $\sim 1000$  km. Nonetheless, there are differences between distributions for these stations as well. So, at the lower-latitude station MSTK, the equatorial distribution boundary is shifted to lower latitudes. Of the two high-latitude maxima (near the meridian of the station centered at  $\Phi \approx 76^\circ$  and the polar one), the first one dominates for MSTK; and the second, for FSMI.

### 2.2. Amplitude and frequency distributions

Let us examine the Earth/satellite amplitude ratio. Figure 3 shows empirical probability density functions

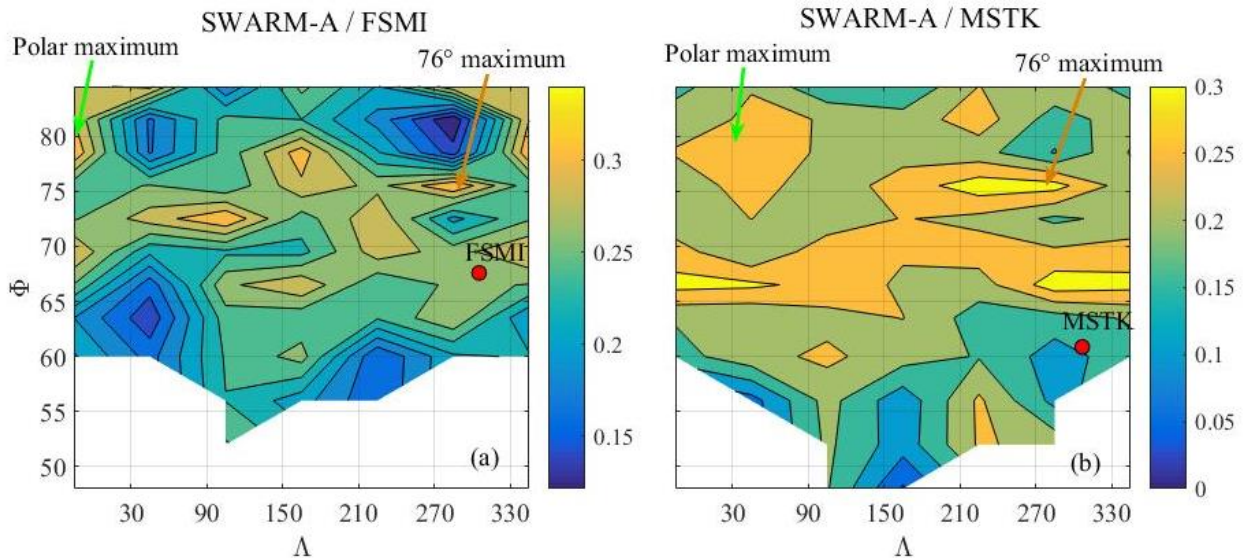


Figure 2. Ratio  $C_{GI}$  defined for a cell  $\Phi$ - $\Lambda$  for two-station pairs as the ratio of the total duration of intervals with coherent oscillations in the ionosphere and on Earth to the total duration of intervals for which spectral analysis was performed. Maxima of  $C_{GI}$  near  $\Phi = 76^\circ$  and near the pole are indicated by arrows

PDF of  $R_{GI}$  for the selected coherent oscillations. The total number of intervals for one pair of components is from 400 to 1000.  $R_{GI}$  varies from  $10^{-4}$  to  $10^{-1}$ , and the most likely values differ for the two stations and for the components on Earth. For the auroral station FSMI, the  $R_{GI}$  distribution median for the latitudinal component on Earth and both components in the ionosphere is  $(3 \div 5) \cdot 10^{-3}$ , whereas for the meridional one,  $(5 \div 8) \cdot 10^{-2}$ , i.e. approximately by an order of magnitude higher. At the subauroral station MSTK, the  $R_{GI}$  distribution maximum for both components is within  $(1 \div 2) \cdot 10^{-2}$ , but for the latitudinal component the distribution is enriched with small values of  $R_{GI}$ . At the PINA and THRF stations (not shown in Figure 3), the contrast between the components disappears and the most probable values of  $R_{GI}$  are within  $(2 \div 5) \cdot 10^{-2}$ . The oscillations recorded in the ionosphere at geomagnetic latitudes above  $72^\circ$  and at distances between a satellite footprint and a station from 1500 to 3000 km make the greatest contribution to the distributions considered.

Figure 4 illustrates frequency distributions of spectral maxima for the FSMI and MSTK stations. The spectral maxima of coherent oscillations are observed throughout the frequency range considered with predominant frequencies above 6 Hz and distribution maxima near 8 and 11 Hz. Next, we will figure out how the Earth/satellite pulsation amplitude ratio determined from measurements correlate with model estimates depending on the beam radius.

## 3. COMPARISON BETWEEN OBSERVED AND CALCULATED $R_{GI}$

To analyze the spatial structure of the wave field on Earth and in the ionosphere, we have employed the model of Alfvén beam passage through a quasi-real ionosphere [Fedorov et al., 2018]. This model can calculate spatial distributions of magnetic and electric fields in the ionosphere and on Earth for an Alfvén beam of finite radius

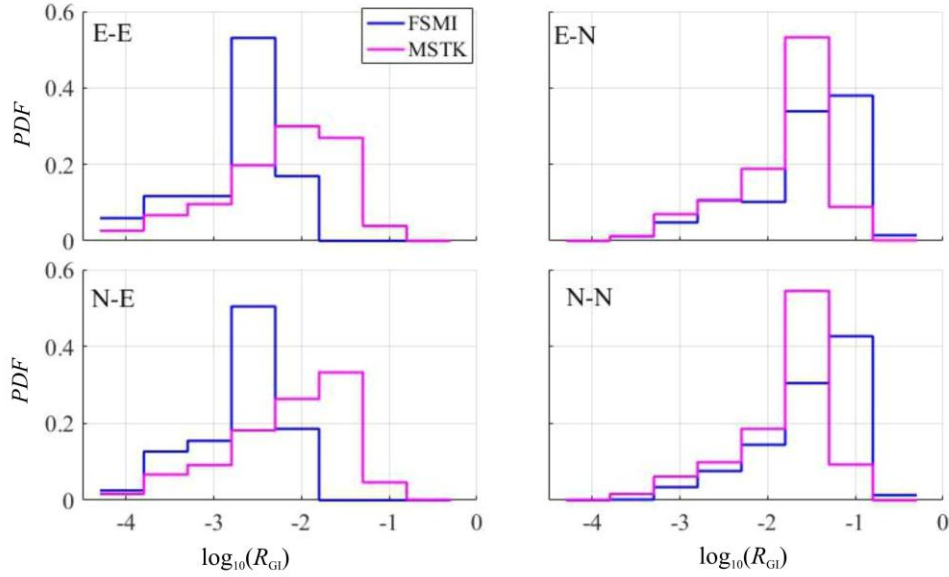


Figure 3. Empirical distribution functions  $PDF$  for the Earth/ionosphere amplitude ratio  $R_{GI}$  for the same two stations as in Figure 2. The component pair is designated as follows: E-N:  $B_E$  (ionosphere),  $B_N$  (Earth)

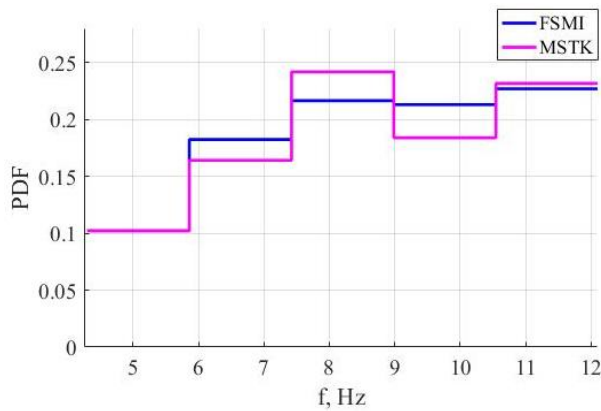


Figure 4. Distribution of coherent oscillations over frequencies of spectral maxima of  $B_N$  in the ionosphere

radius incident on the ionosphere. The incident wave has a beam structure with a nonzero radial component of electric field and an azimuthal component of magnetic field such that the dependence on the radial distance  $\rho$  from the center of the beam has the form  $B_\phi \sim \rho/\rho_0 \exp(-(\rho/\rho_0)^2 + 1)$ .

The vertical profile of ionospheric parameters was found using IRI-2007 [Bilitza, Reinisch, 2008] supplemented by MSIS for the neutral atmosphere [Hedin et al., 1977; Emmert et al., 2020]. In the Hz frequency range, the spectral and spatial distributions of the magnetic field in the ionosphere depend on the presence of IAR and waveguides for fast magnetosonic (FMS) waves. Two main spatial scales are given by the Alfvén velocity profile and the beam radius.

To obtain the dependence of the field amplitude on the radial distance  $B(\rho)$ , the summation is taken over spatial harmonics. The spectrum shape is influenced by the oscillation frequency, the beam radius, and the complex dielectric permeability profile in the ionosphere, which depends mainly on the solar flux level. Thus, such IRI input parameters as season, local solar time LT, and latitude have an effect on the spatial distribution of magnetic field in the ionosphere and on

Earth. Due to satellite orbit precession, oscillations were recorded in September in the evening (18 LT) and morning (6 LT) sectors; and in December, in the pre-noon (10–11 LT) and pre-midnight (22–23 LT) sectors.

The dependence of the amplitude of magnetic field components on the radial distance from the beam axis in the ionosphere at the SWARM orbit height and on Earth is demonstrated in Figure 5 for a period near the equinox in the dawn sector. The geographical latitude of the beam center is  $70^\circ$ ; 8 and 11 Hz frequencies are considered for two values of beam radius. In the ionosphere, for a beam with  $\rho_0 = 200$  km, the amplitudes of both horizontal components are close at short distances from the beam axis, and with  $\rho > 2000$  km they differ no more than by an order of magnitude with predominant radial and azimuthal components at 11 Hz and 8 Hz respectively. A maximum amplitude is observed at a distance of  $\sim \rho_0$  from the axis (the exact value depends on the beam radius and frequency). For the problem we deal with, it is essential that at a radial distance from the maximum, the amplitude changes by about an order of magnitude.

An incident Alfvén beam can excite waves in both ionospheric and atmospheric waveguides. Due to interference of these modes, the amplitude-distance dependence  $B(\rho)$  has a nonmonotonic form. The  $B(\rho)$  function on Earth and in the ionosphere can be represented as a sum of slowly changing  $B_0(\rho)$  and oscillating  $b(\rho)$ , which, in view of the interference, is not strictly periodic, so we can only talk about a mean spatial period.  $B_0(\rho)$  decreases rapidly at distances up to several beam radii, and then the decrease slows down sharply. At large distances,  $B_0(\rho)$  is greater for a beam of larger radius. For both values of the oscillation frequency and the beam radius at large distances from the axis, the radial component dominates on Earth, and the amplitude for the azimuthal component is by 1–2 orders of magnitude lower.

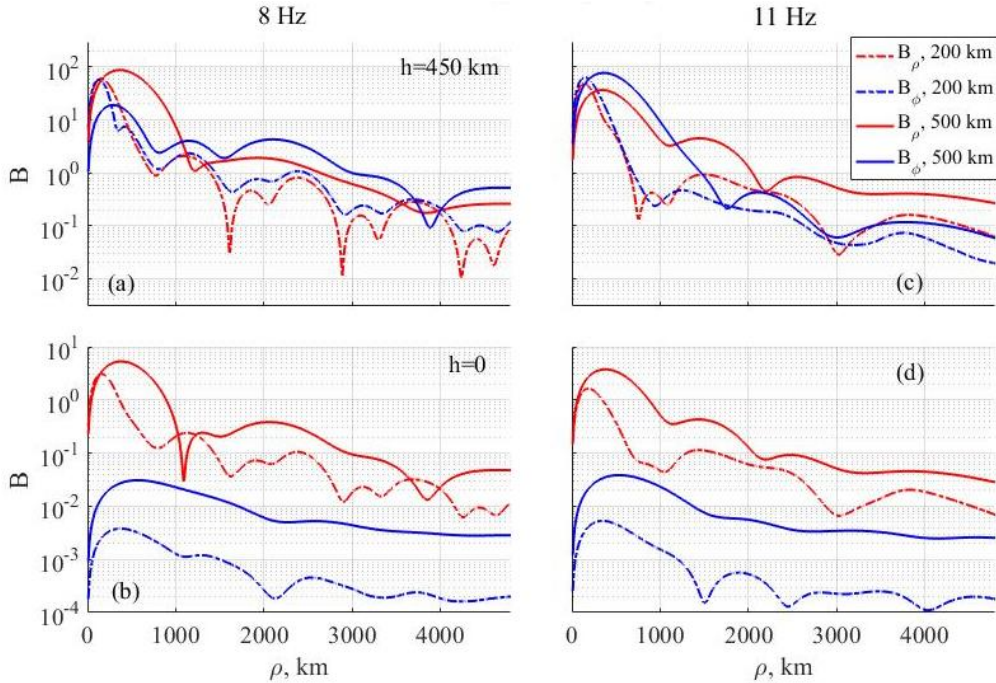


Figure 5. Calculated radial distance dependence of the amplitude of horizontal magnetic field components in the ionosphere (top panels) and on Earth (bottom panels) for an incident Alfvén beam with a frequency of 8 Hz (a, b) and 11 Hz (c, d) in the dawn sector near the equinox. Geographic latitudes of the beam center are given in the title; the radius, in the legend

With an increase in the beam radius, the mean spatial period  $\langle \lambda^* \rangle$  of the oscillating function  $b(\rho)$  increases both in the ionosphere and on Earth. As a result, the oscillations become smoother, and the relative amplitude of variations decreases in the ionosphere (Figure 5, a). Spatial variations are smoothed both when passing through the ionosphere so that  $B(\rho)$  on Earth becomes smoother (see Figure 5, a, b) than in the ionosphere, and as the frequency increases (Figure 5, a–c and b–d).

Quantitative differences between distributions at different levels of ionospheric illumination are reduced to variations in the amplitude and spatial period  $\langle \lambda^* \rangle$  of  $b(\rho)$  in the ionosphere and on Earth. Figure 6 plots  $\langle \lambda^* \rangle$  of  $b_\rho(\rho)$  as a function of beam radius  $\rho_0$  on Earth for a frequency of 6 Hz and a geographic latitude of  $70^\circ$ . Both near equinoxes and near solstices,  $\langle \lambda^* \rangle$  is  $\sim 500$  km at  $\rho_0 = 100$  km and increases approximately twice with increasing beam radius from 100 to 400 km, but the increase depends on the level of illumination in the ionosphere. At the lowest level of illumination (night hours, December), the increase at small beam radii is slow; with an increase in illumination, the increase in the initial part is more rapid, and at  $\rho_0 > 300$  km the dependence attains the saturation.

To figure out how the values of the Earth/ionosphere amplitude ratio obtained from observations agree with the model ones, we analyze the dependence  $R_{GI}$  on the radial distance at a frequency of 8 Hz for all local time and season combinations for different beam radii. Since the amplitudes are close for the two components at the height of the satellite at short distances from the axis,  $R_{GI}$  was calculated as the amplitude ratio of one of the components on Earth to the meridional component in the ionosphere. There is uncertainty in determining the ratio  $R_{GI}$  since the exact distance from the center of the beam in the ionosphere to the satellite is unknown. Engebretson et al. [2008] for Pc1

pulsations in the ionosphere have shown that the maximum peak-to-peak amplitude of these oscillations exceeds 10 nT. Similar values have been obtained in [Yagova et al., 2023] for the magnetic field oscillations in the range 2.5–10 Hz, and the most probable peak-to-peak amplitudes of oscillations in the ionosphere, for which a signal is observed on Earth, are  $\sim 1$  nT. Given that in the ionosphere the amplitude decreases by an order of magnitude at an approximately beam radius distance from the amplitude maximum, which is observed at  $\rho \approx \rho_0$ , we calculate the ratio  $R_{GI}$  for  $\rho = 2\rho_0$ .

The results are presented in Figure 7 for September (left) and December (right). The highest  $R_{GI}$  is peculiar to night conditions near the winter solstice (Figure 7, c). For  $B_p$  and  $\rho_0 = 500$  km  $R_{GI} > 0.1$  at  $\rho < 2000$  km, and at large distances  $R_{GI}$  does not fall below  $5 \cdot 10^{-2}$ . At  $\rho_0 = 200$  km,  $R_{GI}$  is several times lower than for  $\rho_0 = 500$  km, but

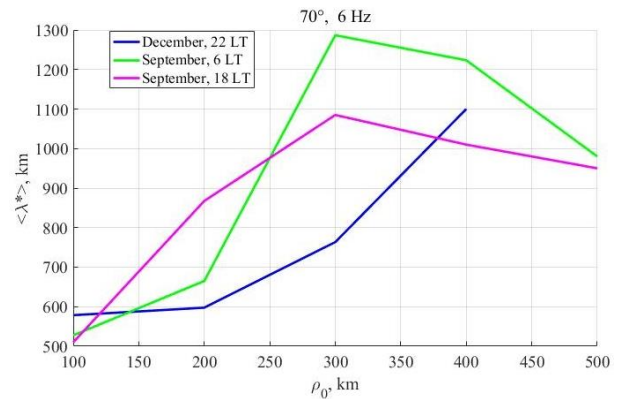


Figure 6. Mean spatial period  $\langle \lambda^* \rangle$  of the radial component  $b_\rho(\rho)$  of  $b(\rho)$ , determined from  $\rho > 2\rho_0$  on Earth, as a function of beam radius for a frequency of 6 Hz and a geographic latitude of  $70^\circ$

even in this case  $R_{GI}$  remains higher than  $10^{-2}$  everywhere except in the vicinity of the minima. For the azimuthal component,  $R_{GI}$  is almost two orders of magnitude lower than for the radial one. A qualitatively similar pattern is observed near the equinox for both morning (Figure 7, *a*) and evening (Figure 7, *b*) conditions, but  $R_{GI}$  for the dominant meridional component becomes lower as the electron density increases. In September in the dawn sector at  $\rho=2000$  km,  $R_{GI}=5\cdot 10^{-2}$ , and at large distances the values decrease to  $10^{-3}$ . In the dusk sector,  $R_{GI}$  is about an order of magnitude lower than in the dawn one. Common to all these cases are large values for a larger beam radius and the dominance of the radial component  $B_\rho$  at large distances from the beam axis. On Earth, the azimuthal component  $B_\phi$  can be neglected since its amplitude is by 1–2 orders of magnitude lower than that of  $B_\rho$ .

Qualitative differences from the cases considered are observed in the dayside sector in December (Figure 7, *d*). If for  $\rho_0=200$  km the radial component  $B_\rho$  is dominant as in the previous cases, at  $\rho_0\geq 500$  km at large distances  $B_\phi$  begins to dominate, and in the radial component there is an inverse dependence of  $R_{GI}$  on beam radius:  $R_{GI}$  for  $\rho_0\geq 500$  km becomes lower than for  $\rho_0\leq 300$  km. The effect increases with increasing beam radius, and at large distances from the beam axis  $R_{GI}$  for  $B_\rho$  of a narrow beam and  $B_\phi$  of a wide one becomes comparable. To illustrate this effect, Figure 7, *d* for daytime conditions in December shows  $R_{GI}(\rho)$  for  $\rho_0=700$  km. The  $R_{GI}$  values decrease to  $10^{-2}$  at distances to  $3\rho_0$ , and at  $\rho>2000$  km the radial component of the narrow beam and the azimuthal component of the wide beam, for which  $R_{GI}\approx 10^{-3}$ , “survive”.

Thus, for all season and local time combinations considered at distances from 1000 to 3000 km from the beam axis, maximum  $R_{GI}$  for the dominant component ranges from  $5\cdot 10^{-4}$  to  $2\cdot 10^{-1}$ . Analysis of coherent oscillations in

the ionosphere and on Earth shows that for most intervals the  $R_{GI}$  values found from measurements are in the same range (see Figure 3).

Choose the intervals when coherent pulsations are recorded simultaneously in the ionosphere and at several ground stations. For each of these events, the beam radius remains constant and we can analyze the amplitude dependence on radial distance. Most of such pulsations occurred in December: in the night sector in the vicinity of 8 Hz ( $8\pm 0.6$  Hz) and in the daytime at  $f\approx 8$  and 11 Hz. The results for the night sector are shown in Figure 8. Since the model predicts the dominance of the radial component relative to the beam axis on Earth, we assume that it completely determines the amplitude on Earth. For the ionospheric regions where the probability of coherent oscillations is maximum (arrows in Figure 2 indicate maxima near  $\Phi=76^\circ$  and near the pole), the radial component in the system associated with the beam coincides almost precisely with the meridional one on Earth. Table 2 lists values of  $\mu=\cos(\psi)$ , where  $\psi$  is the angle between the magnetic meridian and the direction to the beam center, and  $\psi_{\max}$  is the location of the satellite when the beam axis is shifted by  $2\rho_0$  in longitude from the meridian of the station. Even in this case,  $\mu$  is close to 1.

Geographic latitudes of satellites ranged from  $69^\circ$  to  $72.5^\circ$ , the latitude of  $70^\circ$  was used for the calculation. Calculated  $R_{GI}(\rho)$  for  $B_\rho$  for three beam radius values is shown by curves; and observed one, by markers. Distances between a satellite footprint and a station range from 1700 to 3000 km; and  $R_{GI}$ , from  $10^{-2}$  to  $10^{-1}$ . For most of the events,  $R_{GI}$  correspond to the calculated values in the range of beam radii considered.

The results for daytime conditions are presented in Figure 9. For the events in the left panel, the frequencies

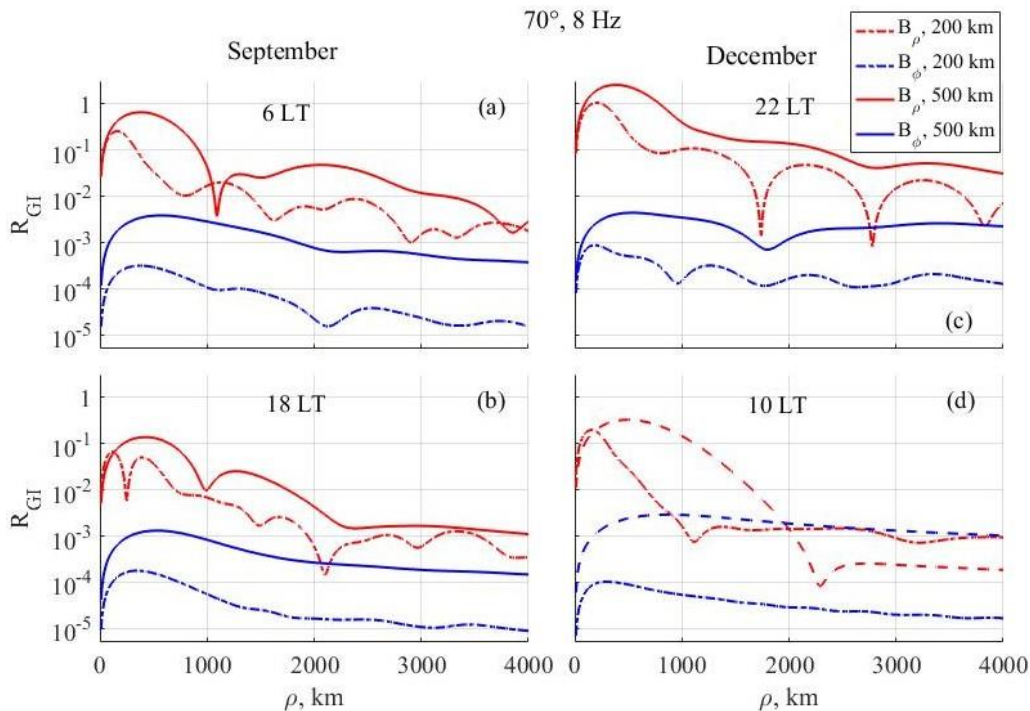


Figure 7. Calculated dependence of  $R_{GI}$  on radial distance for a frequency of 8 Hz near the equinox (*a*, *b*) and solstice (*c*, *d*)

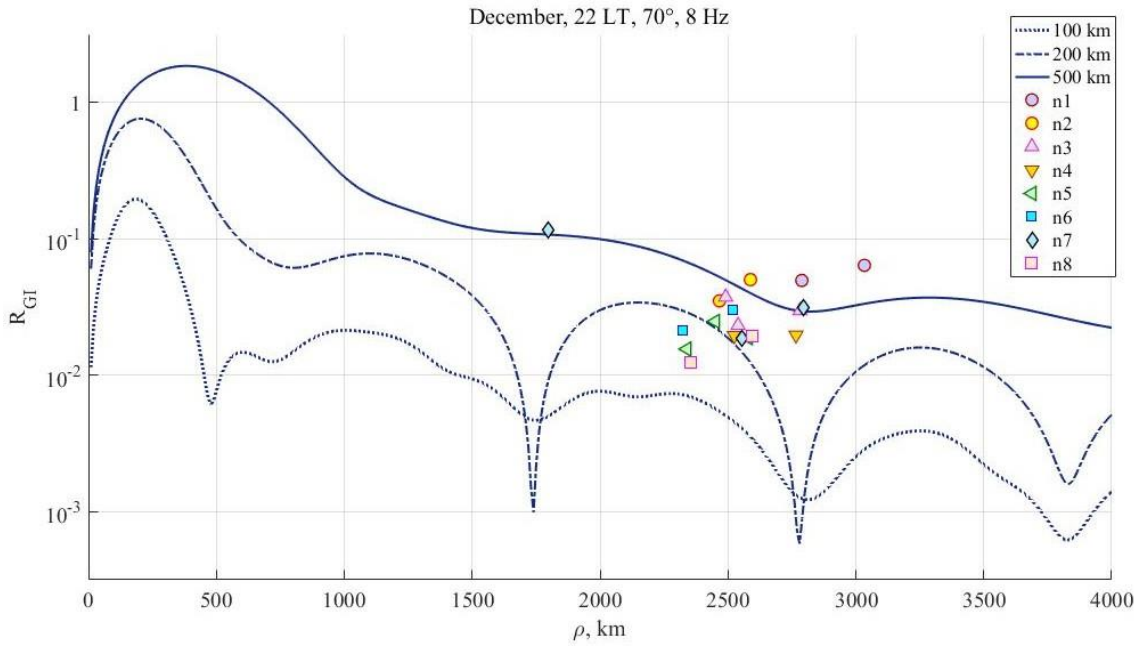


Figure 8. Comparison between calculated and measured  $R_{GI}$  for night conditions in December

Table 2

Parameters of main maxima of occurrence of coherent oscillations in the ionosphere and on Earth, shown in Figure 2

Station (Figure)	Maximum	Geographic coordinates		Corrected geomagnetic coordinates		$\mu = \cos(\psi_{max})$
		latitude	longitude	latitude, $\Phi$	longitude, $\Lambda$	
FSMI (2, a)	76°	70°	243°	76°	295°	0.78
	near-polar	74°	289°	81°	5°	0.92
MSTK (2, b)	76°	78°	195°	76°	240°	0.89
	near-polar	74°	305°	79°	40°	0.93

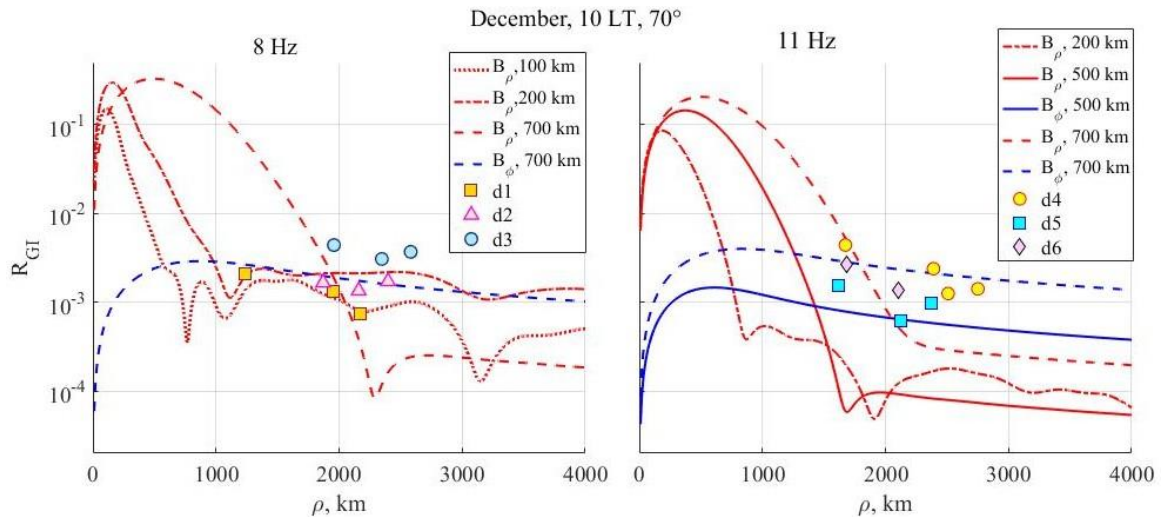


Figure 9. Comparison of calculated and measured  $R_{GI}$  for daytime conditions in December at 8 Hz (left) and 11 Hz (right)

range from 7.4 to 9 Hz; and geographic latitudes of the satellite, from 69° to 71°. Distances vary from 1200 to 2700 km; and  $R_{GI}$ , from  $6 \cdot 10^{-4}$  to  $5 \cdot 10^{-3}$ , which approximately corresponds to calculated values for the dominant component. For daytime conditions near the winter solstice, close calculated values can fit both the azimuthal component for the wide beam

and the radial component for the narrow one. For instance,  $R_{GI}$  in event d1 fits better  $B_\rho$  at  $100 < \rho_0 < 200$  km, and for event d2 both interpretations are almost equal. At the same time, event d3 more closely corresponds to the wide beam ( $\rho_0 \geq 700$  km), for which the radial component dominates at small distances; and the azimuthal component, at large distances.

The right panel of Figure 9 presents the results for  $f=11$  Hz. Oscillation frequencies range from 10.9 to 12.1 Hz; and satellite's geographic latitudes, from  $68^\circ$  to  $72.6^\circ$ . Distances between the stations and the satellite footprint vary from 1600 to 2800 km; and  $R_{GI}$ , from  $5 \cdot 10^{-4}$  to  $5 \cdot 10^{-3}$ . Thus, ranges of  $R_{GI}$  for 8 and 11 Hz coincide, but for 11 Hz these values are in line with the calculated ones only for a wide beam.

#### 4. DISCUSSION

The Earth/ionosphere amplitude ratio  $R_{GI}$  at frequencies above the nominal Pc1 range corresponds to an Alfvén beam incident on the ionosphere with a radius of several hundred kilometers. Since the maximum of occurrence of such oscillations in the ionosphere is at latitudes higher than those of ground stations, and the distance along the meridian between the maximum zone and ground stations exceeds 1000 km, to the radial component  $B_p$  approximately corresponds the meridional component on Earth. Note that when amplitudes of the components differ by an order of magnitude or more, which occurs in the model at large distances from the beam axis, the azimuthal component can be completely neglected and the behavior of both components on Earth is controlled by the radial component. An additional error associated with the difference between the direction to the beam center and the orientation of the corresponding component on Earth is smaller than that arising from uncertainty in localizing the beam from satellite data. Thus, it makes sense to compare calculated and measured  $R_{GI}$  to estimate the order of magnitude. Diagnostic capabilities are improved for individual events when coherent oscillations are recorded simultaneously in the ionosphere and at several ground points, and the large latitude difference between a satellite and a ground station reduces the impact of the error associated with inaccurate localization of the beam center. Evidence that the model as a whole correctly describes the oscillations recorded in the ionosphere and on the ground is not only the coincidence of the  $R_{GI}$  ranges calculated and reconstructed from measurement data, but also the same dependence on local time. As in model calculations,  $R_{GI}$  determined from measurements at night is approximately by an order of magnitude higher than that during the day.

The model predicts the dominance of the radial component on Earth and high  $R_{GI}$  for large beam radii. Such dependence occurs for all ionospheric conditions considered, except for daytime hours near the winter solstice. For these conditions, a qualitative difference arises between narrow and wide beams. For the narrow beam, the radial component dominates at large distances, as under other conditions in the ionosphere; for the wide one, the radial component dominates at small distances from the beam axis; and the azimuthal component, at large distances. Furthermore, at large distances from the beam axis, close values of  $R_{GI} \sim 10^{-3}$  occur in the radial component for the narrow beam and in the azimuthal component for the wide one, which makes the interpretation of measurement data ambiguous. This ambiguity is partly due to the limited data available and can be eliminated by increasing the number of satellites

and ground stations and including not only amplitude but also phase distribution in the analysis. There are, however, restrictions of the model as well. The use of IRI at high latitudes is limited to intervals of low auroral activity when the contribution of precipitation to ionospheric conductivity in the E layer is small. The selected events generally fit this condition, but correct consideration of precipitation can change the derived amplitudes and  $R_{GI}$ .

Moreover, the model ignores variations in ionospheric parameters between the beam and the ionospheric projection of the ground station and inside the beam for wide beams. Near the auroral oval and terminator boundaries, the horizontal irregularity of the ionosphere becomes significant, accounting for which will require a significant modification of the model. Indirect evidence for this is the revealed features of the wave amplitude distribution during the daytime near the winter solstice. Since in winter at high latitudes a sunlit region is a narrow band near noon, for a wide beam an error associated with the approximation of a horizontally homogeneous ionosphere can significantly affect the results.

The complex dielectric permeability profile in the ionosphere depending on wave frequency [Fedorov et al., 2018], the boundary between narrow and wide beams at which the component dominant at large distances changes depends not only on ionospheric parameters, but also on frequency. So, at  $f=11$  Hz, the beam behaves as wide already at  $\rho_0=300$  km, and at  $f=6$  Hz  $B_p$  also remains dominant when  $\rho_0=500$  km. A source of the discrepancies between model  $R_{GI}$  values and those recovered from measurements may be the difference between oscillation spectra. The model considers one frequency, and the real signal is a short wave packet with broadband spectrum. Taking into account the finite width of the spectrum can lead to noticeable changes if the frequency dependence is strong enough, such as during the daytime near the winter solstice.

#### CONCLUSIONS

The presence of coherent magnetic field oscillations in the ionosphere and on Earth at 4–12 Hz frequencies confirms that the magnetic field variations detected by satellites [Yagova et al., 2023] at frequencies above the nominal Pc1 range are oscillations whose frequencies differ little when recorded by a low-orbit satellite and on Earth.

In the ionosphere, the maximum probability occurs at high geomagnetic latitudes corresponding to polar cusp-cleft regions and the auroral oval polar boundary.

The spatial scale of the oscillations in the ionosphere is hundreds of kilometers, which is confirmed by comparing the values of the Earth/ionosphere amplitude ratio  $R_{GI}$  recovered from measurements and calculated in the model [Fedorov et al., 2018] of propagation of an Alfvén beam of finite radius through the quasi-real ionosphere.

The work was performed under government assignment of IPE RAS (all authors) and GC RAS (V.A. Pilipenko). Magnetic field measurement data from SWARM satellites is available on the website of the European Space Agency (ESA) [<https://swarm-diss.eo.esa.int/>]; and CARISMA measurement data, on the website [<https://www.carisma.ca/about-carisma>].

## REFERENCES

- Allen R.C., Zhang J.-C., Kistler L.M., Spence H.E., Lin R.-L., Klecker B., Dunlop M.W., André M., Jordanova V.K. A statistical study of EMIC waves observed by Cluster: 1. Wave properties. *J. Geophys. Res.: Space Phys.* 2015, vol. 120, pp. 5574–5592. DOI: [10.1002/2015JA021333](https://doi.org/10.1002/2015JA021333).
- Belyaev P.P., Bosinger T., Isaev S.V., Trakhtengerts V.Y., Kangas J. First evidence at high latitude for the ionospheric Alfvén resonator. *J. Geophys. Res.* 1999, vol. 104, pp. 4305–4318.
- Bilitza D., Reinisch B. International Reference Ionosphere. Improvements and new parameters. *Adv. Space Res.* 2008, vol. 42, pp. 599–609. DOI: [10.1016/j.asr.2007.07.048](https://doi.org/10.1016/j.asr.2007.07.048).
- Emmert J.T., Drob D.P., Picone J.M., Siskind D.E., Jones M., Mlynczak M.G., et al. NRLMSIS 2.0: A whole-atmosphere empirical model of temperature and neutral species densities. *Earth and Space Science.* 2020, vol. 8, e2020EA001321. DOI: [10.1029/2020EA001321](https://doi.org/10.1029/2020EA001321).
- Engebretson M.J., Posch J.L., Westerman A.M., Otto N.J., Slavin J.A., Le G., Strangeway R.J., Lessard M.R. Temporal and spatial characteristics of Pc1 waves observed by ST5. *J. Geophys. Res.* 2008, vol. 113, A07206. DOI: [10.1029/2008JA013145](https://doi.org/10.1029/2008JA013145).
- Ermakova E.N., Yakhnin A.G., Yakhnina T.A., Demekhov A.G., Kotik D.S. Sporadic geomagnetic pulsations at frequencies up to 15 Hz in the magnetic storm of November 7–14, 2004: features of the amplitude and polarization spectra and their connection with ion-cyclotron wave in the magnetosphere. *Radiophys Quantum El.* 2016, vol. 58, pp. 547–560. DOI: [10.1007/s11141-016-9628-3](https://doi.org/10.1007/s11141-016-9628-3).
- Fedorov E.N., Pilipenko V.A., Engebretson M.J., Hartinger M.D. Transmission of a magnetospheric Pc1 wave beam through the ionosphere to the ground. *J. Geophys. Res.: Space Phys.* 2018, vol. 123, pp. 3965–3982. DOI: [10.1029/2018JA025338](https://doi.org/10.1029/2018JA025338).
- Hedin A.E., Reber C.A., Newton G.P., Spencer N.W., Brinton H.C., Mayr H.G., Potter W.E. A global thermospheric model based on mass spectrometer and incoherent scatter data MSIS. 2. Composition. *J. Geophys. Res.* 1977, vol. 82, pp. 2148–2156. DOI: [10.1029/JA082i016p02148](https://doi.org/10.1029/JA082i016p02148).
- Jenkins G., Watts D. Spectral analysis and its applications, Holden-Day, San Francisco, London, Amsterdam, 1969, 525 p.
- Le G., Chi P.J., Strangeway R.J., Slavin J.A. Observations of a unique type of ULF wave by low-altitude Space Technology 5 satellites. *J. Geophys. Res.* 2011, vol. 116, A08203. DOI: [10.1029/2011JA016574](https://doi.org/10.1029/2011JA016574).
- Mann I.R., Milling D.K., Rae I.J., Ozeke L.G., Kale A., Kale Z.C., Murphy K.R., et al. The upgraded CARISMA magnetometer array in the THEMIS era. *Space Sci Rev.* 2008, vol. 141, pp. 413–451. DOI: [10.1007/s11214-008-9457-6](https://doi.org/10.1007/s11214-008-9457-6).
- Olsen N., Friis-Christensen E., Floberghagen R., Alken P., Beggan C.D., Chulliat A., et al. The Swarm satellite constellation application and research facility (SCARF) and Swarm data products. *Earth Planets Space.* 2013, vol. 64, pp. 1189–1200. DOI: [10.5047/eps.2013.07.001](https://doi.org/10.5047/eps.2013.07.001).
- Papitashvili V.O., Papitashvili N.E., King J.H. Magnetospheric geomagnetic coordinates for space physics data presentation and visualization. *Adv. Space Res.* 1997, vol. 20, pp. 1097–1100. DOI: [10.1016/S0273-1177\(97\)00565-6](https://doi.org/10.1016/S0273-1177(97)00565-6).
- Polyakov S.V., Rapoport V.O. Ionospheric Alfvén resonator. *Geomagnetism and Aeronomy.* 1981, vol. 21, pp. 816–822.
- Rème H., Aoustin C., Bosqued J.M., et al. First multi-spacecraft ion measurements in and near the Earth’s magnetosphere with the identical Cluster ion spectrometry (CIS) experiment. *Ann. Geophys.* 2001, vol. 19, pp. 1303–1354. DOI: [10.5194/angeo-19-1303-2001](https://doi.org/10.5194/angeo-19-1303-2001).
- Vines S.K., Allen R.C., Anderson B.J., Engebretson M.J., Fuselier S.A., Russel, C.T., et al. EMIC waves in the outer magnetosphere: Observations of an off-equator source region. *Geophys. Res. Lett.* 2019, vol. 46, pp. 5707–5716. DOI: [10.1029/2019GL082152](https://doi.org/10.1029/2019GL082152).
- Yagova N.V., Fedorov E.N., Pilipenko V.A., Mazur N.G., Martines-Bedenko V.A. Geomagnetic variations in the frequency range 2.5–12 Hz in the ionospheric F layer as measured by SWARM satellites. *Solar-Terr. Phys.* 2023, vol. 9, iss. 1, pp. 34–46. DOI: [10.12737/stp-91202305](https://doi.org/10.12737/stp-91202305).
- Yakhnin A.G., Yakhnina T.A., Frey H.U. Subauroral proton spots visualize the Pc1 source. *J. Geophys. Res.* 2007, vol. 112, A10223. DOI: [10.1029/2007JA012501](https://doi.org/10.1029/2007JA012501).  
URL: <https://swarm-diss.esa.int/> (accessed January 11, 2023).
- URL: <https://www.carisma.ca/about-carisma> (accessed January 11, 2023).

*This paper is based on material presented at the 18th Annual Conference on Plasma Physics in the Solar System, February 6–10, 2023, IKI RAS, Moscow.*

Original Russian version: Yagova N.V., Fedorov E.N., Pilipenko V.A., Mazur N.G., published in *Solnechno-zemnaya fizika*. 2023. Vol. 9. Iss. 3. P. 128–137. DOI: [10.12737/szf-93202314](https://doi.org/10.12737/szf-93202314). © 2023 INFRA-M Academic Publishing House (Nauchno-Izdatelskii Tsentr INFRA-M)

### How to cite this article

Yagova N.V., Fedorov E.N., Pilipenko V.A., Mazur N.G. Natural electromagnetic oscillations in 4–12 Hz frequency range as measured by SWARM satellites and CARISMA magnetometer network. *Solar-Terrestrial Physics*. 2023. Vol. 9. Iss. 3. P. 118–126. DOI: [10.12737/stp-93202314](https://doi.org/10.12737/stp-93202314).